**PCCP**

# Giant photonic spin Hall effect induced by hyperbolic shear polaritons

## PCCP

# Giant photonic spin Hall effect induced by hyperbolic shear polaritons

Guangyi Jia,*[a] Wenxuan Xue,[a] Zhenxin Jia,[a] Mathias Schubert*[b]

Recently, broken symmetry within crystals has been igniting tremendous research interest since it can be utilized to effectively manipulate the propagation of photons. In particular, low-symmetry Bravais crystals can support hyperbolic shear polaritons (HShPs), holding great promise for technological upgrading on the emerging research area of spinoptics. Herein, an Otto-type multilayer structure consisting of KRS5 prism, sensing medium, and monoclinic $\beta$-Ga$_2$O$_3$ crystal is designed to ameliorate the photonic spin Hall effect (PSHE). The surface of $\beta$-Ga$_2$O$_3$ is the monoclinic (010) plane (x-y plane). We show that giant spin Hall shifts with three (or two) orders of magnitude of the incident wavelength are obtained in the in-plane (or transverse) directions. The azimuthal dispersions of photonic spin Hall shifts present non-mirror-symmetric patterns at tuning the rotation angle of $\beta$-Ga$_2$O$_3$ around the z axis in plane. All of these exotic optical properties are closely correlated with the broken crystal lattice symmetry and the incurred excitation of HShPs in monoclinic $\beta$-Ga$_2$O$_3$ crystal. By virtue of the remarkably enhanced PSHE, our proposed Otto-type multilayer structure shows a superior biosensing performance in which the maximum sensitivity is two orders of magnitude larger than previously reported PSHE biosensors based on two-dimensional materials. In addition, the optimized physical and structural parameters including the incident angle, excitation wavelength, azimuth angle and doping concentration of $\beta$-Ga$_2$O$_3$, thickness and refractive index of sensing medium are also investigated and given. This work unequivocally confirms the strong influence of crystal symmetry on the PSHE, shedding important insights into understanding the rich modulation of spin-orbit interaction of light via shear polaritons and therefore facilitating potential applications in photoelectronic devices.

## Introduction

The photonic spin Hall effect (PSHE) is an optical analogy of electronic spin Hall effect and its inherent physical mechanism is the spin-orbit interaction of light, which delineates the mutual influence of the spin (circular polarization) and the trajectory of light beam.[1-5] When a linearly polarized light propagates in an inhomogeneous medium, the components with the opposite spins drift along the opposite directions perpendicular to the refractive-index gradient, causing the light beam to split into two circularly polarized beams separated on either side of the incident plane. The spin-dependent splitting in the PSHE is sensitive to the state of the incident photons and the physical parameters of the interface, thus it holds great promise for various applications, such as the biosensor, optical differential manipulation, image processing, and precision metrology, and so forth.[6-10] Unfortunately, the PSHE is typically very weak and the spin-dependent displacements are always at the subwavelength scale, severely inhibiting its practical applications.[11,12]

Until now, even if many strategies including polarization control,[13] anisotropic impedance mismatching,[14] constructing surface plasmonic platform[15] and various metastructures[16-18] have been proposed to enhance the PSHE, the largest photonic spin Hall shifts achieved by these methods are only hundreds of times of the incident wavelength. Besides, the element materials in most of previously reported modulation methods preserve the time-reversal symmetry such that the Hall conductivity (equivalently the off-diagonal permittivity element) is generally zero.[13-18] In our recent studies, we have shown that the PSHE can be greatly enhanced via breaking the time-reversal symmetry of system.[19-21] Particularly, the in-plane spin-dependent shift can be theoretically increased to more than 1000 times of the incident wavelength in a monolayer of black phosphorus with a nonzero Hall conductivity.[21] Nevertheless, rigorous physical conditions (e.g., intense magnetic field, ultralow temperature, and appropriate straining) are necessary for our previously reported model systems, which are difficult to be realized in practical observations.[19-21] In consequence, it is significant to exploit naturally low-symmetry crystalline materials to manipulate the PSHE.

Recently, the low-symmetry Bravais crystal $\beta$-Ga$_2$O$_3$, which is endowed with nontrivial relative orientation (neither parallel nor orthogonal) of several optical transitions, has spurred tremendous research interest due to its non-orthogonal principal crystal axes.[22,23] Especially, the discovering of hyperbolic shear polaritons (HShPs) in monoclinic $\beta$-Ga$_2$O$_3$ further inspires new

[a.] School of Science, Tianjin University of Commerce, Tianjin 300134, P. R. China. Email: gyjia87@163.com
[b.] Department of Electrical and Computer Engineering, University of Nebraska-Lincoln, Lincoln, Nebraska 68588, USA. Email: schubert@engr.unl.edu
†Electronic Supplementary Information (ESI) available: calculation method for the permittivity tensor of $\beta$-Ga$_2$O$_3$, original color maps of photonic spin Hall shifts, photonic spin Hall shifts at $\varepsilon_{xy}$ = 0.0, imaginary parts of $\varepsilon_{xx}$, $\varepsilon_{yy}$, $\varepsilon_{zz}$ and $\varepsilon_{xy}$, the largest photonic spin Hall shifts and their corresponding incident angles, wavelengths, and types of HShPs at different doping concentrations. See DOI: 10.1039/x0xx00000x

This journal is © The Royal Society of Chemistry 20xx

*Phys. Chem. Chem. Phys.*, 2023, **00**, 1-7 | **1**

directions for nanophotonics in low-symmetry materials.[23-26] The HShPs are a new class of polariton modes, which were first proposed and experimentally confirmed by N. C. Passler et al in 2022.[23] They emerge in crystalline materials in which the permittivity tensor cannot be diagonalized. They have been directly observed by near-field real-space nanoimaging and preliminarily shown remarkable potential for enhancing the near-field thermal radiation.[27,28] Even so, the study on HShPs is in its infancy, and lots of new directions including the modulation of PSHE by the HShPs have not yet been explored thus far.

Propelled by the advances in PSHE and natural hyperbolic polaritons, in the present work, we theoretically propose a new method to colossally amend the PSHE. Giant photonic spin Hall shifts are demonstrated in an Otto-type multilayer structure of KRS5 prism/sensing medium/$\beta$-Ga$_2$O$_3$, which are ascribed to the broken crystal lattice symmetry and the related excitation of HShPs in monoclinic $\beta$-Ga$_2$O$_3$ crystal. Furthermore, evolutions of in-plane and transverse spin-dependent displacements with various factors (e.g., incident angle, excitation wavelength, azimuth angle and doping concentration of $\beta$-Ga$_2$O$_3$, thickness and refractive index of sensing medium) are clearly unveiled. Finally, the biosensing performance of our proposed model system is also inspected in detail.

## Model system and the theoretical method

There are five different polymorphisms of bulk Ga$_2$O$_3$, i.e., $\alpha$-, $\beta$-, $\gamma$-, $\sigma$-, and $\varepsilon$-Ga$_2$O$_3$.[29] Among them, $\beta$-Ga$_2$O$_3$ is the most thermodynamically stable phase. $\beta$-Ga$_2$O$_3$ belongs to the C2/m (or C$_{2h}^3$) space group (number 12) and has a base centered monoclinic crystal structure, as shown in Fig. 1(a). The unit cell contains four Ga$_2$O$_3$ molecules and has two crystallographically different Ga atoms. The Ga(I) ions are at tetrahedral sites (with four oxygen neighbors) and the Ga(II) ions are at octahedral sites (with six oxygen neighbors). These low-symmetry Bravais lattices make $\beta$-Ga$_2$O$_3$ exhibit non-orthogonal principal crystal axes. As a result, the dielectric permittivity tensor of $\beta$-Ga$_2$O$_3$ has

major polarizability directions which are strongly dependent on the wavelength $\lambda$, with off-diagonal terms that cannot be completely removed through coordinate rotation. The wavelength-dependent permittivity of $\beta$-Ga$_2$O$_3$ can be described as a third-rank tensor with identical off-diagonal elements

$$\overline{\overline{\varepsilon}} = \begin{bmatrix} \varepsilon_{xx} & \varepsilon_{xy} & 0 \\ \varepsilon_{yx} & \varepsilon_{yy} & 0 \\ 0 & 0 & \varepsilon_{zz} \end{bmatrix} \tag{1}$$

The monoclinic permittivity tensor consists of the high-frequency contributions, the dipole charge resonances, and the free charge-carrier contributions. Its main calculation equations are given in eqn (S1)-(S6) in the ESI†, and its detailed parametrization and calculation method are available in ref. 22.

Fig. 2 presents the optical spectra of diagonal and off-diagonal permittivity elements $\varepsilon_{xx}$, $\varepsilon_{yy}$, $\varepsilon_{zz}$ and $\varepsilon_{xy}$ at a free charge-carrier density $N = 1 \times 10^{18}$ cm$^{-3}$. The parameters of anisotropic charge carrier mobility are $\mu_x = 296$ cm$^2$V$^{-1}$s$^{-1}$ and $\mu_y = \mu_z = 37$ cm$^2$V$^{-1}$s$^{-1}$. In general, the hyperbolic polaritons can be produced when either the real part of one diagonal permittivity element is negative and the other two are positive or two are negative and one is positive. Nonetheless, the strong dielectric response of off-diagonal elements ($\varepsilon_{xy} = \varepsilon_{yx} \neq 0$) in monoclinic $\beta$-Ga$_2$O$_3$ crystal typically prevents the electromagnetic propagation angle from being aligned with the principal axes, giving rise to a remarkable shearing effect of polariton modes. This shear phenomenon in the dielectric response results in extreme anisotropic propagation of surface waves, supporting a polariton class of HShPs.[23]

The dispersion isofrequency contours (IFCs) of HShPs at a frequency $\omega$ with a momentum ($k_x$, $k_y$, $k_z$) can be obtained via solving the Maxwell equations as follows[27]

$$\boldsymbol{k}(\boldsymbol{k} \cdot \boldsymbol{E}) - k^2 \boldsymbol{E} + k_0^2 \overline{\overline{\varepsilon}} \cdot \boldsymbol{E} = 0 \tag{2}$$

where $\boldsymbol{E} = [E_x, E_y, E_z]^T$, $k$ and $k_0$ are the wave vectors in $\beta$-Ga$_2$O$_3$ and vacuum, respectively. The dispersion relation including the IFCs can thus be calculated by

$$\begin{aligned} k_z^4 \varepsilon_{zz} - k_z^2 k_0^2 [\varepsilon_{zz}(\varepsilon_{xx} + \varepsilon_{yy})k_0^2 - \varepsilon_{zz}k_x^2 - \varepsilon_{zz}k_y^2 \\ -(\varepsilon_{xx}k_x^2 + \varepsilon_{yy}k_y^2 + 2\varepsilon_{xy}k_xk_y)] + (\varepsilon_{zz}k_0^2 - k_x^2 - k_y^2)[\varepsilon_{xx}\varepsilon_{yy}k_0^2 \\ -\varepsilon_{xy}^2 k_0^2 - (\varepsilon_{xx}k_x^2 + \varepsilon_{yy}k_y^2 + 2\varepsilon_{xy}k_xk_y)] = 0 \end{aligned} \tag{3}$$

In the experimental model, an Otto-type prism-coupling geometry is designed to excite the HShPs, as sketched in Fig. 1(b). The incident medium and substrate are KRS5 glass prism and bulk $\beta$-Ga$_2$O$_3$, respectively. The KRS5 glass has a good transparency in the spectral range from 5 to 40 $\mu$m and its refractive index is derived from[30]

$$\begin{aligned} n_{\text{KRS5}} = \Bigg( 1 + \frac{1.8293958\lambda^2}{\lambda^2 - 0.0225} + \frac{1.6675593\lambda^2}{\lambda^2 - 0.0625} + \frac{1.1210424\lambda^2}{\lambda^2 - 0.1225} \\ + \frac{0.04513366\lambda^2}{\lambda^2 - 0.2025} + \frac{12.380234\lambda^2}{\lambda^2 - 27089.737} \Bigg)^{1/2} \end{aligned} \tag{4}$$

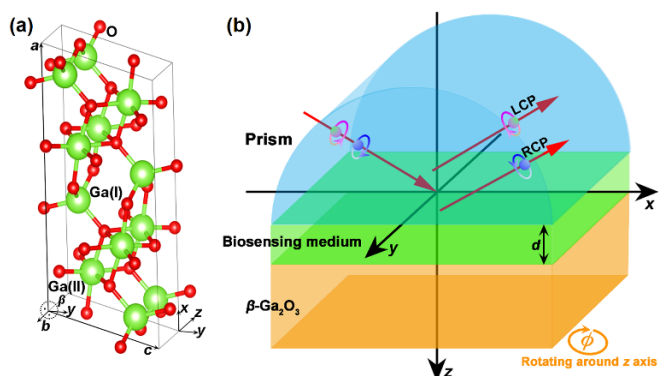There is a biosensing medium with a micron-sized thickness $d$ to



**Fig. 1** (a) Monoclinic crystal structure of $\beta$-Ga$_2$O$_3$ (monoclinic angle $\beta$ = 103.7°). (b) Schematic diagram of an Otto-type HShPs coupling configuration for the modulation of PSHE. LCP and RCP stand for left- and right-circular polarization components of electromagnetic wave, respectively.
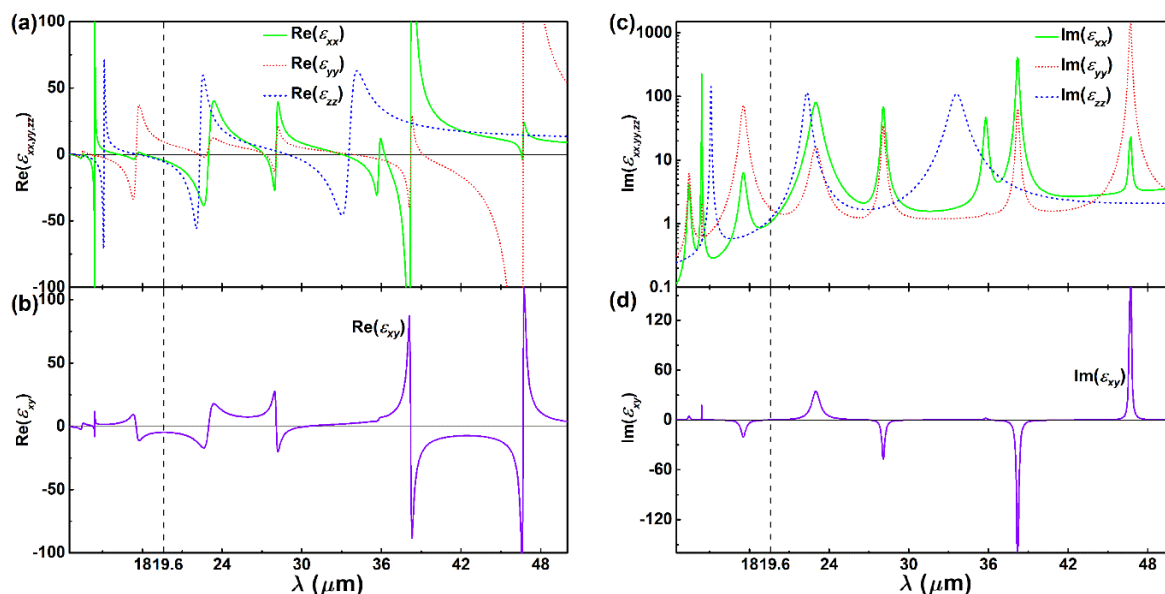
2 | *Phys. Chem. Chem. Phys.*, 2023, **00**, 1-7

This journal is © The Royal Society of Chemistry 20xx

**Fig. 2** (a)(b) Real and (c)(d) imaginary parts of permittivity elements $\varepsilon_{xx}$, $\varepsilon_{yy}$, $\varepsilon_{zz}$, $\varepsilon_{xy}$ for the monoclinic $\beta$-Ga$_2$O$_3$ crystal. The free charge-carrier density is fixed at $N = 1 \times 10^{18}$ cm$^{-3}$. The position of $\lambda = 19.6$ μm at which the in-plane and transverse photonic spin Hall shifts have their respective maximum displacements is marked by dash lines.

be sandwiched between the prism and $\beta$-Ga$_2$O$_3$. The refractive index of the initial calibration biosensing medium is $n_s = 1.419$, corresponding to the organic solvent of ethyl acetoacetate. Hereafter, unless explicitly specified, the thickness of biosensing medium is set as 8.3 μm.

It is assumed that one Gaussian wave packet with a monochromatic wavelength impinges from the prism upon the surface of biosensing medium with an incident angle $\theta_i$. The coordinate system used to define the optical response of $\beta$-Ga$_2$O$_3$ is illustrated Fig. 1. To evaluate the influence of azimuth angle $\phi$ on the PSHE, we also tune the rotation angle of $\beta$-Ga$_2$O$_3$ around the $z$ axis in plane. In the spin basis set, the linearly polarized state of electromagnetic wave can be decomposed into two orthogonal spin components, i.e., the left- and right-circular polarization (LCP and RCP) components.[21,31] Under the paraxial approximation, spin-dependent Hall shifts of these two orthogonal components in reflected beam can be mathematically derived.[31] The PSHE is sensitive to the polarization states of incident photons. We inspect the condition that incident photons are only p-polarized in this work. The corresponding in-plane and transverse spin Hall shifts for LCP and RCP components, as indicated in Fig. 1(b), are given by[21,31]

$$\delta_x^{|\pm\rangle} = \mp \frac{1}{k_i} \text{Re} \left( \frac{r_{pp}}{r_{pp}^2 + r_{sp}^2} \frac{\partial r_{sp}}{\partial \theta_i} - \frac{r_{sp}}{r_{pp}^2 + r_{sp}^2} \frac{\partial r_{pp}}{\partial \theta_i} \right) \quad (5)$$

$$\delta_y^{|\pm\rangle} = \mp \frac{\cot \theta_i}{k_i} \text{Re} \left( \frac{r_{pp} + r_{ss}}{r_{pp}^2 + r_{sp}^2} r_{pp} - \frac{r_{ps} - r_{sp}}{r_{pp}^2 + r_{sp}^2} r_{sp} \right) \quad (6)$$

where $k_i$ is the wave vector in the incident medium, the superscripts $|+\rangle$ and $|-\rangle$ indicate the LCP and RCP components, respectively. Because $\delta_{x,y}^{|+\rangle} = -\delta_{x,y}^{|-\rangle}$, we will only analyze the

photonic spin Hall shifts for LCP component in the following. The Fresnel reflection coefficients $r_{pp}$, $r_{sp}$, $r_{ss}$, and $r_{ps}$ can be calculated via using a generalized $4 \times 4$ transfer matrix formalism for light propagation in anisotropic stratified media.[32,33]

## Results and discussions

We first consider the influence of the incident angle $\theta_i$ and the wavelength $\lambda$ on the PSHE. Fig. 3(a) and (b) show variations of the Fresnel reflection coefficients $|r_{pp}|$ and $|r_{sp}|$ with respect to the $\theta_i$ and $\lambda$. The azimuth angle of $\beta$-Ga$_2$O$_3$ is set to be $\phi = 90°$. One can see from Fig. 3(a) that the $|r_{pp}|$ gives the minimum value 0.0044 at $\theta_i = 26.9°$ and $\lambda = 29.2$ μm. The emergence of nonzero $|r_{sp}|$ in Fig. 3(b) signifies that the reflected light becomes elliptically polarized, and both orientation angle and ellipticity of reflected polarization state change with the incident angle.[21,34] The incident angles at which the reflection of p-polarized light is nearly extinguished correspond to the Brewster's angles. Fig. 3(a) demonstrates that the Brewster's angles are diverse for different $\lambda$ values.

Previous studies have shown that photonic spin Hall shifts are sensitive to the minimum values of $|r_{pp}|$ such that they generally give extreme values around the Brewster's angles.[19-21] This change rule is reproduced through comparing Fig. 3(a) with Fig. 3(c-d). Especially, the $\delta_x^{|+\rangle}$ (or $\delta_y^{|+\rangle}$) gives the largest displacement of -1200$\lambda$ (or 279.2$\lambda$) at $\theta_i = 28.1°$ and $\lambda = 19.6$ μm. In order to increase the color contrast, the color scales of $\delta_x^{|+\rangle}$ and $\delta_y^{|+\rangle}$ in Figs. 3 and 6-8 are limited in smaller ranges. Original color maps of $\delta_x^{|+\rangle}$ and $\delta_y^{|+\rangle}$ are shown in Figs. S1-S4 in the ESI†. At $\lambda = 19.6$ μm, the real part of permittivity element $\varepsilon_{yy}$ is positive
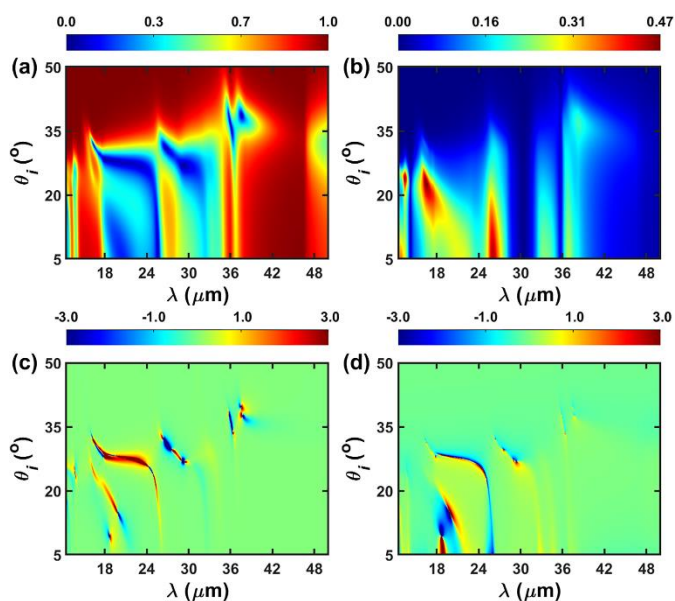
**Fig. 3** Variations of the Fresnel reflection coefficients (a) $|r_{pp}|$ and (b) $|r_{sp}|$ with respect to the incident angle $\theta_i$ and the wavelength $\lambda$ of excitation light. (c) In-plane and (d) transverse spin-dependent shifts versus the parameters of $\theta_i$ and $\lambda$. The color bars in (a)(b) are unitless while they are scaled in the unit of $\lambda$ in (c)(d).



**Fig. 4** (a) Real parts of permittivity elements $\varepsilon_{xx}$, $\varepsilon_{yy}$, $\varepsilon_{zz}$ and $\varepsilon_{xy}$ and (b) the IFCs of HShPs at $k_z = 0$ for the monoclinic $\beta$-Ga$_2$O$_3$ crystal at different doping concentrations $N$ (in cm$^{-3}$). The wavelength is $\lambda = 19.6$ μm. In (a), the symbols are the calculated results while solid lines are just drawn as a guide to the eye. The inset in (a) shows partially magnified profiles for clarity.

while those of the other three ($\varepsilon_{xx}$, $\varepsilon_{zz}$, and $\varepsilon_{xy}$) are negative [see Fig. 2(a-b)], indicating that the $\beta$-Ga$_2$O$_3$ crystal supports type II in-plane HShPs.[23] After artificially setting the off-diagonal permittivity element $\varepsilon_{xy}$ of $\beta$-Ga$_2$O$_3$ to be zero (the other factors are the same with those of Fig. 3), the maximum shift of $\delta_x^{|+\rangle}$ (or $\delta_y^{|+\rangle}$) decreases to -24.7$\lambda$ (or 60.1$\lambda$), as shown in Fig. S5 in the ESI†. This further verifies that the giant photonic spin Hall shifts in Fig. 3 are induced by off-diagonal-term-incurred HShPs.

HShPs stem from the nontrivial relative orientation (neither parallel nor orthogonal) of several optical transitions which contribute to a net polarization (cannot be aligned with the crystal axes) at a given frequency. As a result, even in the rotated coordinate system, the permittivity tensor of $\beta$-Ga$_2$O$_3$ has off-diagonal terms associated with shear phenomena. The PSHE originates from the presence of permittivity gradient. The off-diagonal terms of monoclinic $\beta$-Ga$_2$O$_3$ crystal contribute more degrees of freedom to permittivity variation gradient, which can effectively enhance the PSHE. Besides, previous study has shown that the largest displacement of one spin component can be up to only half of Gaussian beam waist.[35] In practical experiment, thus, the beam waist should be large enough in order to observe the displacement with three orders of magnitude of the incident wavelength.

Fig. 4(a) shows the real parts of $\varepsilon_{xx}$, $\varepsilon_{yy}$, $\varepsilon_{zz}$ and $\varepsilon_{xy}$ as a function of the electron-doping concentration $N$ in monoclinic $\beta$-Ga$_2$O$_3$ crystal at $\lambda = 19.6$ μm. The corresponding imaginary parts are shown in Fig. S6 in the ESI†. Because the permittivity elements meet Re($\varepsilon_{xx,zz,xy}$) < 0 and Re($\varepsilon_{yy}$) > 0, the $\beta$-Ga$_2$O$_3$ crystal supports type II in-plane hyperbolic IFCs for all different $N$ values, as shown in Fig. 4(b). Additionally, the values of Re($\varepsilon_{xx}$), Re($\varepsilon_{yy}$)
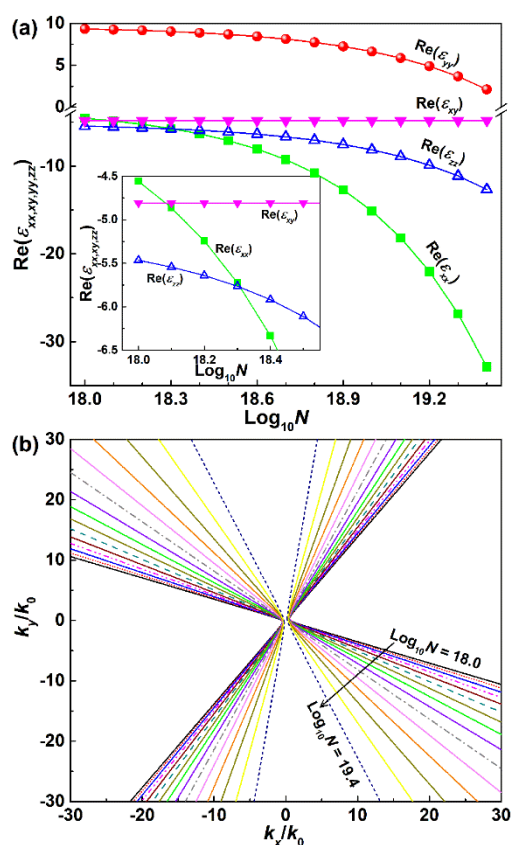
and Re($\varepsilon_{zz}$) gradually decrease as the doping concentration increases. Therefore, not only does the wave-vector magnitude of HShPs change but the direction of hyperbolic IFC also rotates within the monoclinic plane as the doping concentration varies [Fig. 4(b)].

Influenced by the changed permittivity tensor (accompanied by the tuned hyperbolic IFC), the largest values of $\left|\delta_x^{|+\rangle}\right|$ and $\left|\delta_y^{|+\rangle}\right|$ at $\lambda = 19.6$ μm mainly present a decreasing tendency with increasing the doping concentration, as delineated in Fig. 5(a). It is worth noting that the largest value of $\left|\delta_x^{|+\rangle}\right|$ exhibits a 'U' type variation at log$_{10}N$ = 18.1, 18.2, and 18.3. The detailed reason remains to be clarified by a further study. One possible explain is that the increase of free carriers in $\beta$-Ga$_2$O$_3$ leads to an intermediate region at which the values of Re($\varepsilon_{xx}$) locate between those of Re($\varepsilon_{xy}$) and Re($\varepsilon_{zz}$), as shown in the inset in Fig. 4(a). Fig. 5(b) gives the corresponding incident angles of the largest values of $\left|\delta_x^{|+\rangle}\right|$ and $\left|\delta_y^{|+\rangle}\right|$ in Fig. 5(a). One can see that the incident angles of the largest values of $\left|\delta_x^{|+\rangle}\right|$ and $\left|\delta_y^{|+\rangle}\right|$ are nearly equal at log$_{10}N$ = 18.0−18.4 while they will deviate from each other with increasing log$_{10}N$ from 18.5 to 19.4. This variation trend is well in line with that of permittivity tensor for $\beta$-Ga$_2$O$_3$.
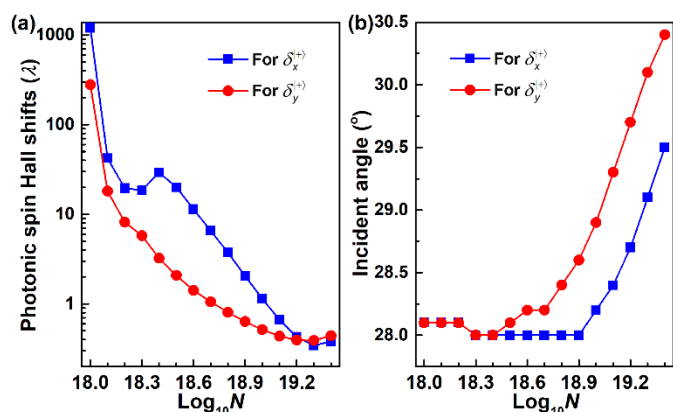
**4** | *Phys. Chem. Chem. Phys.*, 2023, **00**, 1-7

This journal is © The Royal Society of Chemistry 20xx

**Fig. 5** Variations of (a) the largest absolute values of $\delta_x^{|+\rangle}$, $\delta_y^{|+\rangle}$ and (b) the corresponding incident angles with respect to the doping concentrations $N$ (in cm$^{-3}$) of monoclinic $\beta$-Ga$_2$O$_3$ crystal at $\lambda = 19.6$ μm. The symbols are the calculated results while solid lines are just drawn as a guide to the eye.



**Fig. 6** Variations of the Fresnel reflection coefficients (a) $|r_{pp}|$ and (b) $|r_{sp}|$ with respect to the incident angle $\theta_i$ and the azimuth angle $\phi$. (c) In-plane and (d) transverse spin-dependent shifts versus the parameters of $\theta_i$ and $\phi$. The color bars in (a)(b) are unitless while they are scaled in the unit of $\lambda$ in (c)(d).

As shown in Fig. 4(a), Re($\varepsilon_{xx}$), Re($\varepsilon_{xy}$) and Re($\varepsilon_{zz}$) are close to each other and Re($\varepsilon_{yy}$) also slowly changes at $\log_{10}N = 18.0-18.4$. By contrast, the real parts of diagonal permittivity elements dramatically decrease and the deviations between Re($\varepsilon_{xx}$), Re($\varepsilon_{xy}$) and Re($\varepsilon_{zz}$) become increasingly large as the $\log_{10}N$ increases from 18.5 to 19.4.

Fig. 5 intends to unveil the evolution of photonic spin Hall shifts with the doping concentration at a fixed wavelength. In fact, except for $\log_{10}N = 18.0$, the in-plane and transverse spin-dependent shifts for $\log_{10}N = 18.1-19.4$ give their respective maximum values at the other wavelengths rather than $\lambda = 19.6$ μm. Similar to Fig. 3, we have also inspected the variations of $\delta_x^{|+\rangle}$ and $\delta_y^{|+\rangle}$ with respect to the incident angle $\theta_i$ and the wavelength $\lambda$ at $\log_{10}N = 18.1-19.4$. Fig. S7 (or S8) in the ESI† depicts the largest in-plane (or transverse) photonic spin Hall shifts and their corresponding $\theta_i$ and $\lambda$ values for $\log_{10}N = 18.1-19.4$. It is found that the $\delta_x^{|+\rangle}$ (or $\delta_y^{|+\rangle}$) can be also enhanced by nearly three (or two) orders of magnitude of the wavelength for $\log_{10}N = 18.1$ and 19.3 (or $\log_{10}N = 18.2$, 18.3 and 19.3) at certain $\theta_i$ and $\lambda$ values. According to the values of diagonal and off-diagonal permittivity elements, as summarized in table S1 in the ESI†, we may draw a conclusion that the enhancement of PSHE is associated with the HShPs supported by monoclinic $\beta$-Ga$_2$O$_3$ crystal.

We continue to focus on the case of $\log_{10}N = 18.0$ and $\lambda = 19.6$ μm. Fig. 6 exhibits the optical spectra of Fresnel reflection coefficients and photonic spin Hall shifts versus the incident angle $\theta_i$ and the azimuth angle $\phi$. To demonstrate the effects of symmetry breaking of $\beta$-Ga$_2$O$_3$ crystal structure in the PSHE, we also calculate the Fresnel reflection coefficients and photonic spin Hall shifts after artificially setting the off-diagonal permittivity element $\varepsilon_{xy}$ of $\beta$-Ga$_2$O$_3$ to be zero, as shown in Figs. S9 and S10 in the ESI†. It is seen from Figs. S9 and S10 in the ESI† that all the optical spectra of $|r_{pp}|$, $|r_{sp}|$, $\delta_x^{|+\rangle}$ and $\delta_y^{|+\rangle}$ are symmetric about the crystal axes $\phi = 0°$ (180°) and 90°, and the largest in-plane (or transverse) spin-dependent shift is only
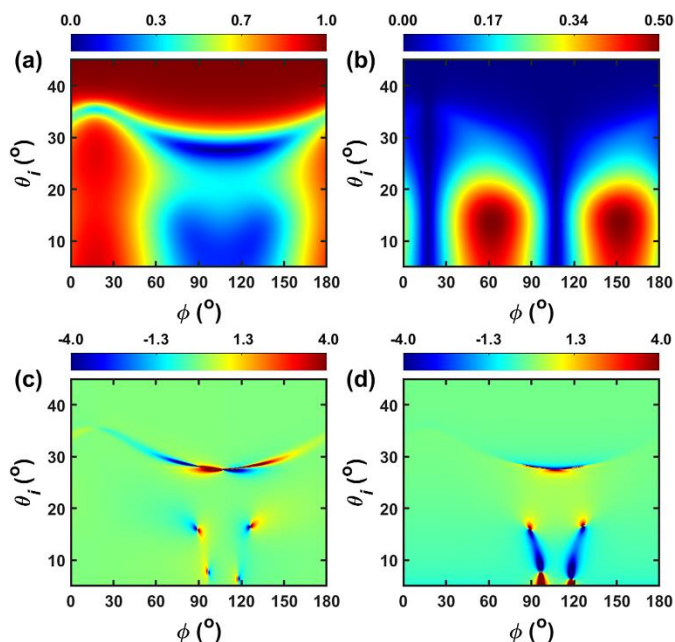
-41.2$\lambda$ (or 28$\lambda$) at $\varepsilon_{xy} = 0.0$. In marked contrast, after taking into account the nonzero $\varepsilon_{xy}$ (Figs. 6 and S2 in the ESI†), all the azimuthal dispersion of Fresnel reflection coefficients and photonic spin Hall shifts exhibits no mirror symmetry, and the largest in-plane (or transverse) spin-dependent shift increases to -1200$\lambda$ (or 279.2$\lambda$) at $\theta_i = 28.1°$ and $\phi = 90°$.

In view of the giant PSHE induced by HShPs, we also examine the biosensing performance of the structure in Fig. 1(b). Figs. 7 and S3 in the ESI† exhibit the Fresnel reflection coefficients and photonic spin Hall shifts at different incident angles and thicknesses $d$ of the biosensing medium. Because of the sensitivity of the minimal value of $|r_{pp}|$ to the $d$ [see Fig. 7(a)], the photonic spin Hall shifts in Fig. 7(c) and (d) are also susceptible to the $d$ around the Brewster's angles, implying that the HShPs tuned PSHE has great potential in detecting the thickness of biosensing medium. In particular, the largest in-plane (or transverse) photonic spin Hall shift of -1200$\lambda$ (or 279.2$\lambda$) appears at $\theta_i = 28.1°$ and $d = 8.3$ μm. This is also the reason why the factor $d$ in the initial model is set as 8.3 μm.

Finally, variations of the Fresnel reflection coefficients and photonic spin Hall shifts with respect to the incident angle $\theta_i$ and the refractive index $n_s$ of biosensing medium are shown in Figs. 8 and S4 in the ESI†. It is seen that the $n_s$ is almost linear with the $\theta_i$ for both $\delta_x^{|+\rangle}$ and $\delta_y^{|+\rangle}$ locating at the incident angles ranging from ~23.8° to ~32.7° [Fig. 8(c) and (d)]. Thus, one can select different refractive-index materials as the sensing medium, and the selection range of $n_s$ covers 1.0−2.0. Here, the largest in-plane (or transverse) spin-dependent shift of -1200$\lambda$ (or 279.2$\lambda$) emerges at $\theta_i = 28.1°$ and $n_s = 1.419$. Fixing the incident angle at 28.1°, the variation of $n_s$ induced via biomolecular concentration

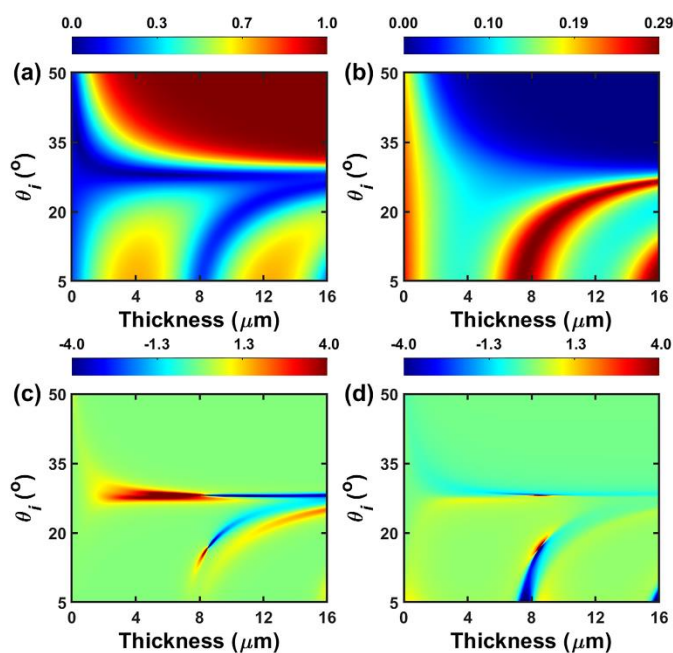**Fig. 7** Variations of the Fresnel reflection coefficients (a) $|r_{pp}|$ and (b) $|r_{sp}|$ with respect to the incident angle $\theta_i$ and the thickness $d$ of biosensing medium. (c) In-plane and (d) transverse spin-dependent shifts versus the parameters of $\theta_i$ and $d$. The refractive index of biosensing medium is $n_s = 1.419$. The color bars in (a)(b) are unitless while they are scaled in the unit of $\lambda$ in (c)(d).
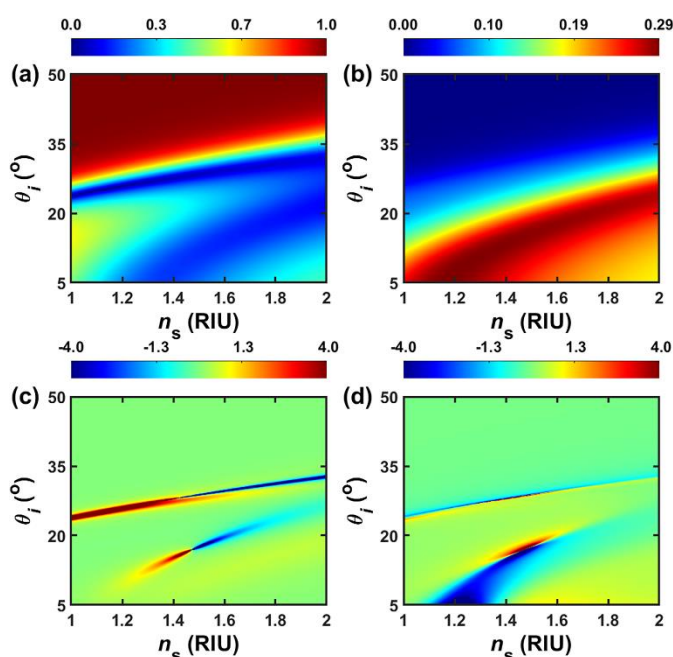


**Fig. 8** Variations of the Fresnel reflection coefficients (a) $|r_{pp}|$ and (b) $|r_{sp}|$ with respect to the incident angle $\theta_i$ and the refractive index $n_s$ of biosensing medium. (c) In-plane and (d) transverse spin-dependent shifts versus the parameters of $\theta_i$ and $n_s$. The color bars in (a)(b) are unitless while they are scaled in the unit of $\lambda$ in (c)(d).

**Table 1** Comparison of the biosensing performance for different multilayered structures of PSHE biosensors

| Structure | Wavelength | Maximum sensitivity | Ref. |
|---|---|---|---|
| BK7 prism/sodium/PMMA/ graphene/sensing medium | 1.2 μm | 1844.9 μm/RIU | 36 |
| BK7 prism/Au/graphene/ sensing medium | 633 nm | $1.088 \times 10^5$ μm/RIU | 37 |
| BK7 prism/Au/BlueP/MoS$_2$/ graphene/sensing medium | 633 nm | $1.555 \times 10^5$ μm/RIU | 38 |
| BK7 prism/graphene/ sensing medium/BK7 glass | 632.8 nm | $6.1 \times 10^5$ μm/RIU | 6 |
| Silicon/Au/magnetic fluid | 1.557 μm | $6.25 \times 10^7$ μm/RIU | 39 |
| KRS5 prism/ sensing medium/$\beta$-Ga$_2$O$_3$ | 19.6 μm | $2.36 \times 10^7$ μm/RIU | This work |

can be accurately measured by observing the change of photonic spin Hall shifts. Because the maximum displacement of $\delta_x^{|+\rangle}$ is far larger than that of $\delta_y^{|+\rangle}$, the biosensing sensitivity based on in-plane spin-dependent shift is calculated by $S_\delta = \Delta \delta_x^{|+\rangle} / \Delta n_s$. And we obtain the maximum sensitivity $2.36 \times 10^7$ μm/RIU at the refractive-index difference $\Delta n_s = 1.419 \text{-} 1.418 = 0.001$. In order to more clearly indicate the advantages of the structure in Fig. 1(b), table 1 compares the biosensing performance of some recently proposed biosensors based on PSHE with ours. It is found that the maximum sensitivity in this work is at least two orders of magnitude larger than those of PSHE biosensors based on two-dimensional materials. Even if the maximum sensitivity of biosensor configuration of silicon/Au/magnetic fluid is a little larger than ours, it has the same order of magnitude with ours. Moreover, the noble metal Au is expensive and the preparation of magnetic fluid is tedious. Thereby, our proposed PSHE biosensor is more superior in consideration of the manufacturing cost.

## Conclusions

To summarize, the enhancement of spin-dependent splitting of reflected light via the HShPs is investigated through designing an Otto-type configuration of KRS5 prism/sensing medium/$\beta$-Ga$_2$O$_3$. We show that the in-plane (or transverse) photonic spin Hall shifts can be amplified to be more than 1000 (or 200) times of the incident wavelength at appropriate structural and physical parameters. Besides, the azimuthal dispersions of photonic spin Hall shifts present non-mirror-symmetric patterns at tuning the rotation angle of $\beta$-Ga$_2$O$_3$ around the $z$ axis in plane. All of these extraordinary merits are attributed to the natural symmetry breaking and the related excitation of HShPs in monoclinic $\beta$-Ga$_2$O$_3$ crystal. By virtue of the giant PSHE, the maximum biosensing sensitivity can reach to $\sim 10^7$ μm/RIU which is at least two orders of magnitude larger than previously reported PSHE

**6** | *Phys. Chem. Chem. Phys.*, 2023, **00**, 1-7

This journal is © The Royal Society of Chemistry 20xx

biosensors based on two-dimensional materials. These findings not only provide new approaches to dramatically manipulate the spin-orbit interaction of light, but may also offer potential for developing novel biosensors to address the label-free detection of ultralow-concentration analytes.

## Conflicts of interest

There are no conflicts to declare.

## Acknowledgements

## Notes and references

1 M. Onoda, S. Murakami and N. Nagaosa, *Phys. Rev. Lett.*, 2004, **93**, 083901.
2 O. Hosten and P. Kwiat, *Science*, 2008, **319**, 787–790.
3 J. Zhou, H. Qian, H. Luo, S. Wen and Z. Liu, *Nanoscale*, 2019, **11**, 17111–17119.
4 J. Ni, S. Liu, Y. Chen, G. Hu, Y. Hu, W. Chen, J. Li, J. Chu, C.-W. Qiu and D. Wu, *Nano Lett.*, 2022, **22**, 9013–9019.
5 B. Song, S.-C. Wen and W. Shu, *ACS Photonics*, 2022, **9**, 3987–3994.
6 J. Cheng, Y. Xiang, J. Xu, S. Liu and P. Dong, *IEEE Sens. J.*, 2022, **22**, 12754–12760.
7 R. Wang, S. He and H. Luo, *Phys. Rev. Appl.*, 2022, **18**, 044016.
8 T. Zhu, Y. Lou, Y. Zhou, J. Zhang, J. Huang, Y. Li, H. Luo, S. Wen, S. Zhu, Q. Gong, M. Qiu and Z. Ruan, *Phys. Rev. Appl.*, 2019, **11**, 034043.
9 M. Kim, D. Lee, Y. Kim and J. Rho, *Nanophotonics*, 2022, **11**, 4591–4600.
10 M. Kim, Y. Yang, D. Lee, Y. Kim, H. Kim and J. Rho, *Laser Photonics Rev.*, 2023, DOI: https://doi.org/10.1002/lpor.202200046
11 G.-Y. Jia, R.-X. Zhang, T. Tang, Q. Li, A. Ebrahimian, Z. Torbatian and R. Asgari, *Phys. Chem. Chem. Phys.*, 2022, **24**, 1877–1884.
12 W. Zhu, H. Zheng, Y. Zhong, J. Yu and Z. Chen, *Phys. Rev. Lett.*, 2021, **126**, 083901.
13 M. Kim, D. Lee, Y. Kim and J. Rho, *Nanophotonics*, 2022, **11**, 2803–2809.
14 M. Kim, D. Lee, H. Cho, B. Min and J. Rho, *Laser Photonics Rev.*, 2021, **15**, 2000393.
15 X. Yu, X. Wang, Z. Li, L. Zhao, F. Zhou, J. Qu and J. Song, *Nanophotonics*, 2021, **10**, 3031–3048.
16 M. Cheng, P. Fu and S. Chen, *Opt. Express*, 2022, **30**, 40075–40086.
17 M. Kim, D. Lee, T. H.-Y. Nguyen, H.-J. Lee, G. Byun and J. Rho, *ACS Photonics*, 2021, **8**, 2705−2712.
18 T. Srivastava, S. Chitriv, S. Sahu, P. Gorai and R. Jha, *J. Appl. Phys.*, 2022, **132**, 203103.
19 G. Jia, R. Zhang, Z. Huang, Q. Ma, H. Wang and R. Asgari, *New J. Phys.*, 2021, **23**, 073010.
20 G. Y. Jia, Z. X. Huang, Q. Y. Ma and G. Li, *Nanophotonics*, 2020, **9**, 715–723.
21 G. Jia, G. Li, Y. Zhou, X. Miao and X. Zhou, *Nanophotonics*, 2020, **9**, 225–233.
22 M. Schubert, R. Korlacki, S. Knight, T. Hofmann, S. Schöche, V. Darakchieva, E. Janzén, B. Monemar, D. Gogova, Q.-T. Thieu, R. Togashi, H. Murakami, Y. Kumagai, K. Goto, A. Kuramata, S. Yamakoshi and M. Higashiwaki, *Phys. Rev. B*, 2016, **93**, 125209.
23 N. C. Passler, X. Ni, G. Hu, J. R. Matson, G. Carini, M. Wolf, M. Schubert, A. Alù, J. D. Caldwell, T. G. Folland and A. Paarmann, *Nature*, 2022, **602**, 595–600.
24 G. Jia, J. Luo, H. Wang, Q. Ma, Q. Liu, H. Dai and R. Asgari, *Nanoscale*, 2022, **14**, 17096–17118.
25 M. Wang, G. Hu, S. Chand, M. Cotrufo, Y. Abate, K. Watanabe, T. Taniguchi, G. Grosso, C.-W. Qiu and A. Alù, *eLight*, 2022, **2**, 12.
26 Q. Zhang, Q. Ou, G. Si, G. Hu, S. Dong, Y. Chen, J. Ni, C. Zhao, M. S. Fuhrer, Y. Yang, A. Alù, R. Hillenbrand and C.-W. Qiu, *Sci. Adv.*, 2022, **8**, eabn9774.
27 G. Hu, W. Ma, D. Hu, J. Wu, C. Zheng, K. Liu, X. Zhang, X. Ni, J. Chen, X. Zhang, Q. Dai, J. D. Caldwell, A. Paarmann, A. Alù, P. Li and C.-W. Qiu, *Nat. Nanotechnol.*, 2023, **18**, 64–70.
28 C.-L. Zhou, G. Tang, Y. Zhang, M. Antezza and H.-L. Yi, *Phys. Rev. B*, 2022, **106**, 155404.
29 R. Roy, V. G. Hill and E. F. Osborn, *J. Am. Chem. Soc.*, 1952, **74**, 719–722.
30 https://refractiveindex.info/?shelf=other&book=TlBr-TlI&page=Rodney
31 W. Zhang, W. Wu, S. Chen, J. Zhang, X. Ling, W. Shu, H. Luo, and S. Wen, *Photonics Res*., 2018, **6**, 511–516.
32 N. C. Passler and A. Paarmann, *J. Opt. Soc. Am. B*, 2017, **34**, 2128–2139.
33 N. C. Passler and A. Paarmann, *J. Opt. Soc. Am. B*, 2019, **36**, 3246-3248.
34 H. Lin, B. Chen, S. Yang, W. Zhu, J. Yu, H. Guan, H. Lu, Y. Luo and Z. Chen, *Nanophotonics*, 2018, **7**, 1929–1937.
35 W. Zhu, J. Yu, H. Guan, H. Lu, J. Tang, J. Zhang, Y. Luo and Z. Chen, *Sci. Rep.*, 2017, **7**, 1150.
36 C. Liang, G. H. Wang, D. M. Deng and T. T. Zhang, *Opt. Express*, 2021, **29**, 29481-29491.
37 X. Zhou, L. Sheng and X. Ling, *Sci. Rep*., 2018, **8**, 1221.
38 A. Srivastava, A. K. Sharma and Y. K. Prajapati, *Chem. Phys. Lett.*, 2021, **774**, 138613.
39 V. A. Popescu, Y. K. Prajapati and A. K. Sharma, *IEEE Trans. Magn.*, 2021, **57**, 4002210.

This journal is © The Royal Society of Chemistry 20xx

*Phys. Chem. Chem. Phys.*, 2023, **00**, 1-7 | **7**